

Fronts, Jets and Vortices

ABSTRACT

When the Rossby number is not small, the dynamics are nonlinear and nonquasi-geostrophic. Such regimes exhibit fronts and jets, the latter being related to the former through pressure gradients. Strong jets meander and shed vortices, which also populate this dynamical regime. The chapter ends with a brief discussion of geostrophic turbulence, the state of many interacting vortices under the influence of Coriolis effects. This problem is particularly well suited to introduce spectral methods for nonlinear problems.

18.1 FRONTS AND JETS

18.1.1 Origin and Scales

A common occurrence in the atmosphere and ocean is the encounter of two fluid masses that, due to separate origins, have distinct properties. The result is the existence of a local transitional region that is relatively narrow (compared with the dimensions of the main fluid masses) and where properties vary spatially more rapidly than on either side. Such a region of intensified gradients of fluid properties is called a *front*.

Typically, the adjacent fluid masses have different densities, and the front is accompanied by a relatively large pressure gradient. Under the action of Coriolis forces, the process of geostrophic adjustment is at work, leading to a relatively intense flow aligned with the front. The weaker density gradients in the main part of each fluid mass confine the motion to the frontal region, and the flow exhibits the form of a jet. The most notable jet in the atmosphere is the so-called polar-front jet stream found around a latitude of 45°N and a few kilometers above sea level (pressure around 300 millibars), at the boundary between subtropical and polar air masses (Fig. 18.1). From the thermal–wind relation

$$f \frac{\partial u}{\partial z} = \frac{g}{\rho_0} \frac{\partial \rho}{\partial y}, \quad (18.1)$$

we can readily see that a weak velocity at sea level must intensify with height to become an intense eastward flow at high altitude. This is because of the general north–south gradient of temperature between the two air masses. In the ocean,

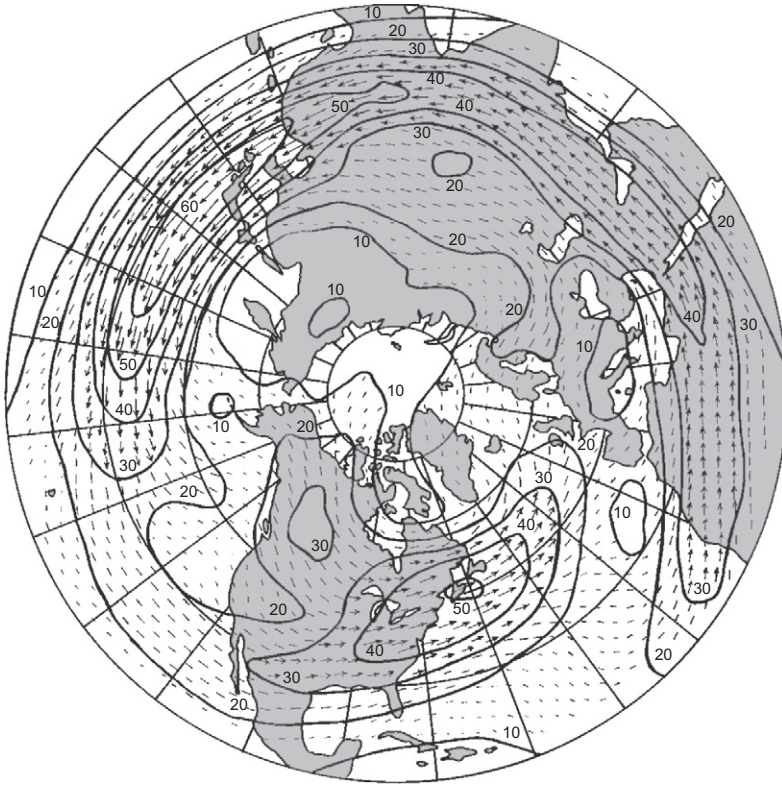


FIGURE 18.1 Monthly winds (in meters per second) over the northern hemisphere for January 1991 at the 300-mb pressure level. Note the jet stream around the 45°N parallel, except over the eastern North Pacific and eastern North Atlantic, where blockings are present. (From National Weather Service, NOAA, Department of Commerce, Washington, D.C.)

a surface-to-bottom front is often found in the vicinity of the shelf break owing to different water properties above the continental shelf and in the deep ocean; such a front is invariably accompanied by currents along the shelf (Fig. 18.2).

According to Section 15.1, the simultaneous presence of a horizontal gradient of density and a vertical gradient of horizontal velocity can yield a thermal–wind balance, which may persist for quite some time. Our earlier discussions of geostrophic adjustment (Section 15.2) demonstrated how such a balance can be achieved following the penetration of one fluid mass into another of different density and indicated that the width of the transitional region is measured by the internal radius of deformation, expressed as

$$R = \frac{NH}{f} \sim \frac{\sqrt{g'H}}{f} \quad (18.2)$$

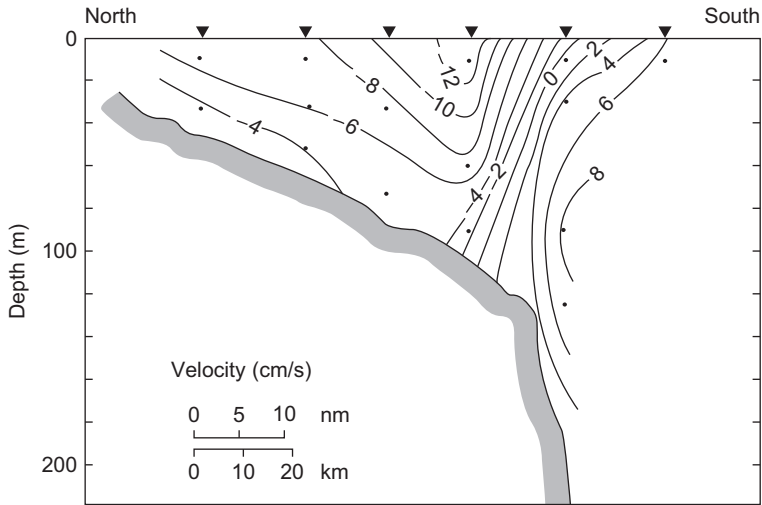


FIGURE 18.2 Monthly mean along-shelf currents for April 1979 across the shelf break on the southern flank of Georges Bank (41°N , 67°W). The units are centimeters per second, and positive values indicate flow pointing into the page. (From Beardsley et al., 1983, as adapted by Gawarkiewicz & Chapman, 1992)

in the respective cases of continuous stratification and layered configuration. Here f is the Coriolis parameter, H is an appropriate height scale (assuming large excursions of density surfaces in frontal systems), N is the stratification frequency, and g' is a suitable reduced gravity. If the density difference between the fluid masses is $\Delta\rho$, the accompanying pressure difference is $\Delta P \sim \Delta\rho gH = \rho_0 g'H$, and, through geostrophy, the velocity scale is

$$U = \frac{\Delta P}{\rho_0 f R} \sim \frac{g'H}{fR} = \sqrt{g'H}. \quad (18.3)$$

From this follows that the internal radius of deformation may also be expressed as $R = U/f$, in which we recognize the inertial-oscillation radius (see Section 2.3). Here, the two coincide because we assume a frontal structure with $\Delta H = H$.

The Froude and Rossby numbers are, respectively

$$Fr = \frac{U}{NH} \sim \frac{\sqrt{g'H}}{fR} \sim 1, \quad (18.4)$$

$$Ro = \frac{U}{fR} \sim \frac{\sqrt{g'H}}{fR} \sim 1, \quad (18.5)$$

and thus both are on the order of unity, implying that the effects of stratification and rotation are equally important within the jet (see Section 11.6).

The jet has a velocity maximum, coinciding more or less with the location of the maximum density gradient, on both sides of which the velocity decays. The corresponding shears form a distribution of relative vorticity that is clockwise on the right and counterclockwise on the left (respectively, anticyclonic and cyclonic in the northern hemisphere). This shear vorticity scales as $Z = U/R \sim f$, which is thus comparable with the planetary vorticity. Note that, if the relative vorticity is strongly anticyclonic, the total vorticity may have the sign opposite to f . Hence, use of conservation of potential vorticity requires some care.

18.1.2 Meanders

Observations reveal that all jets meander, unless they are strongly constrained by the local geography. As a fluid parcel flows in a meander, its path curves, subjecting it to a transverse centrifugal force on the order of $\mathcal{K}U^2$, where \mathcal{K} is the local curvature of the trajectory (the inverse of the radius of curvature). This force can be met by a reduction or increase of the Coriolis force if the parcel's velocity adjusts by ΔU , such that $f\Delta U \sim \mathcal{K}U^2$, or

$$\frac{\Delta U}{U} \sim \frac{\mathcal{K}U}{f} \sim \mathcal{K}R. \quad (18.6)$$

Note that the product $\mathcal{K}R$ is in essence the deformation radius divided by the curvature radius.

In the northern hemisphere ($f > 0$), the Coriolis force acts to the right of the fluid parcel, and thus a rightward turn causing a centrifugal force to the left necessitates a greater Coriolis force and an acceleration ($\Delta U > 0$) (see Fig. 18.3). Similarly, a leftward turn is accompanied by a jet deceleration ($\Delta U < 0$). The reverse conclusions hold for the southern hemisphere, but in each case, the stronger the curvature, the larger the change in velocity, according to Eq. (18.6).

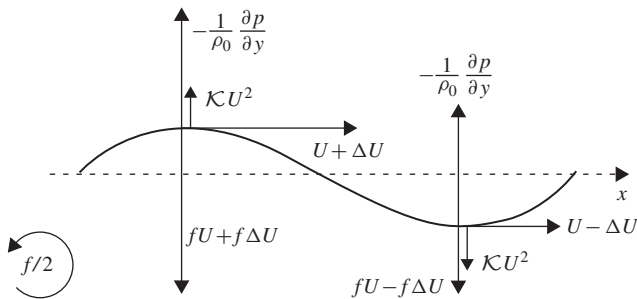


FIGURE 18.3 For the same pressure gradient, a rightward turn requires a larger velocity enabling Coriolis force to balance pressure and centrifugal force. In a left turn, the opposite takes place, and the velocity is reduced.

The same result can be obtained by considering changes in relative vorticity. Neglecting for the moment the beta effect as well as any vertical stretching or squeezing, the relative vorticity is conserved. It can be expressed locally as

$$\zeta = \frac{\partial v}{\partial x} - \frac{\partial u}{\partial y} = \frac{\partial V}{\partial n} - \mathcal{K}V, \quad (18.7)$$

where $V = (u^2 + v^2)^{1/2}$ is the flow speed (scaling as U), n is the cross-jet coordinate (measured positively to the right of the local velocity and scaling as R), and \mathcal{K} is the jet's path curvature (positive clockwise). The first term, $\partial V/\partial n$, is the contribution of the shear and the second, $-\mathcal{K}V$, represents a vorticity due to the turning of the flow. We shall call these contributions shear vorticity and orbital vorticity (See Fig. 18.4 and Analytical Problem 11). In a rightward turn ($\mathcal{K} > 0$), the fluid parcel acquires clockwise orbital vorticity, on the order of $\mathcal{K}U$, which must be at the expense of shear vorticity, $\Delta U/R$. Equating $\mathcal{K}U$ to $\Delta U/R$ again leads to Eq. (18.6).

The change in shear vorticity implies a shift of the parcel with respect to the jet axis. To show this, let us take for example, the fluid parcel that possesses the maximum velocity (i.e., it is on the jet axis) upstream of the meander; there, it has no shear and no orbital vorticity. If this parcel turns to the right in the meander, it acquires clockwise orbital vorticity, which must be compensated by a counterclockwise shear vorticity of the same magnitude. Thus, the parcel must now be on the left flank of the jet. The parcel occupying the jet axis (having maximum velocity and thus no shear vorticity) is one that was on the right flank of the jet upstream and has exchanged its entire clockwise shear vorticity for an equal amount of clockwise orbital vorticity. From this, it is straightforward to conclude that all parcels are displaced leftward with respect to the jet axis in a rightward meander, and rightward with respect to the jet axis in a leftward turn. (This rule is easy to remember: Fluid parcels shift across the jet in the direction of the centrifugal force.)

A consequence of these vorticity adjustments created by meandering is that fluid parcels near the edges may separate from the jet or be captured by it.

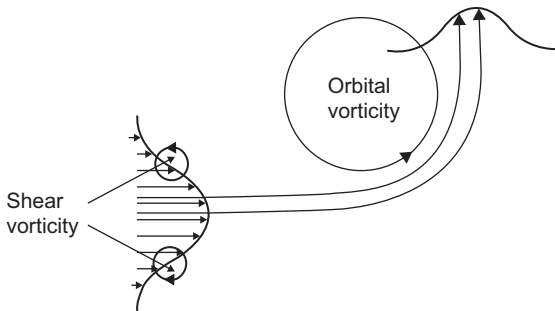


FIGURE 18.4 Difference between shear and orbital vorticity of a jet.

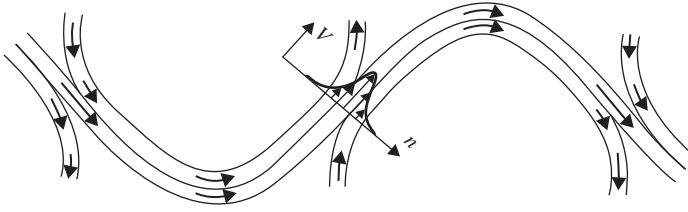


FIGURE 18.5 Separation and capture of fluid parcels along the edges of a meandering jet. This process occurs because the vorticity adjustment required by the meander causes marginal parcels to reverse their velocity. Parcels near the inside edge of the meander see their velocity reversed once curvature has ceased and effectively leave the jet. Similarly, parcels of fluid are joining the jet from the outside at the exit of a meander.

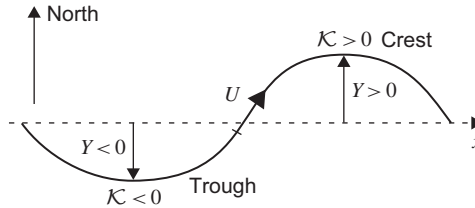


FIGURE 18.6 Meandering of an eastward jet on the beta plane (northern hemisphere). If the meridional displacement Y , curvature \mathcal{K} , and jet speed U are related by $\beta_0 Y \simeq \mathcal{K}U$, changes in planetary and orbital vorticity are comparable and opposite in sign, leaving the velocity profile of the jet (shear vorticity) relatively unperturbed.

Indeed, a parcel on the edge of the jet may have insufficient shear vorticity for trading with orbital vorticity (Fig. 18.5).

The preceding considerations ignored the beta effect, by which the Coriolis force is able to vary. Let us limit ourselves here to the case of an eastward *westerly* jet in the northern hemisphere, which is the case of the atmospheric jet stream and the Gulf Stream in the North Atlantic beyond Cape Hatteras. In a northern meander excursion, called a *crest* (because it appears higher on a map), the curvature is rightward or anticyclonic (Fig. 18.6). The meridional displacement Y , the meander's amplitude, causes an augmentation to the Coriolis force on the order of $\beta_0 YU$, acting to the right of the parcel. However, the centrifugal force on the order of $\mathcal{K}U^2$ acts to its left. Three cases are possible: $\beta_0 Y$ is much less than, on the order of, or much greater than $\mathcal{K}U$.

- If $\beta_0 Y$ is much less than $\mathcal{K}U$, we are in the presence of weak meander amplitudes (small Y) and/or short meander wavelengths (large \mathcal{K}). In this case, the beta effect mitigates the curvature effect but not in a significant way, and the previous conclusions remain qualitatively unchanged.
- If $\beta_0 Y$ is on the order of $\mathcal{K}U$, then the beta and curvature effects can balance each other, leaving the structure of the jet barely affected. For

a sinusoidal meander $Y(x) = A \sin k_x x$, where A is the meander amplitude, $\lambda = 2\pi/k_x$ is its wavelength, and x is the eastward coordinate, we deduce that at the meander's peak ($\sin k_x x = +1$), the meridional displacement Y is A , and the curvature $\mathcal{K} = -[d^2 Y/dx^2]/[1 + (dY/dx)^2]^{3/2}$ is $k_x^2 A$. The balance $\beta_0 Y \sim \mathcal{K} U$ then yields $\beta_0 \sim k_x^2 U$ or

$$\lambda = \frac{2\pi}{k_x} = 2\pi \sqrt{\frac{U}{\beta_0}}. \quad (18.8)$$

From this emerges a particular length scale,

$$L_\beta = \sqrt{\frac{U}{\beta_0}}, \quad (18.9)$$

which we shall call the *critical meander scale*. Cressman (1948) noted its importance in relation to the development of long waves on the atmospheric jet stream, whereas Moore (1963) obtained a solution to an ocean-circulation model that exhibits meanders at that scale. Later, Rhines (1975) demonstrated how this same scale plays a pivotal role in the evolution of geostrophic turbulence on the beta plane.

- In very broad meanders, for which meridional displacements are large and curvatures are small ($\beta_0 Y \gg \mathcal{K} U$), the beta effect dwarfs the curvature effect, and the trade-off is almost exclusively between changes in planetary vorticity and shear vorticity. In a meander crest (greater f), the shear vorticity must become less cyclonic or more anticyclonic (see Fig. 18.7).

Meanders on a jet do not remain stationary but propagate, usually downstream and rarely upstream. The direction of propagation can be inferred from

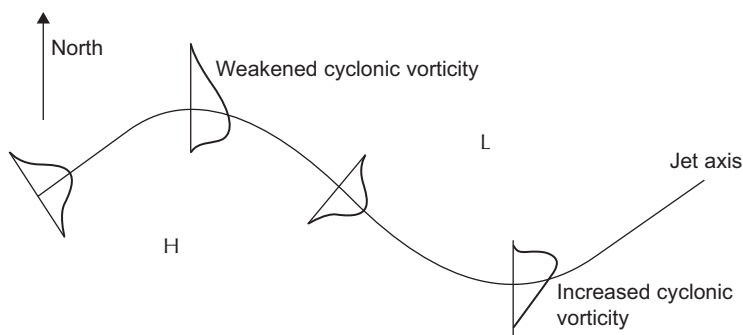


FIGURE 18.7 Changes in shear vorticity in very broad meanders. These are caused by the beta effect, which changes the Coriolis force with latitude. The figure is drawn for the case of south–north displacements in the northern hemisphere. The letters H and L indicate high- and low-pressure regions, respectively.

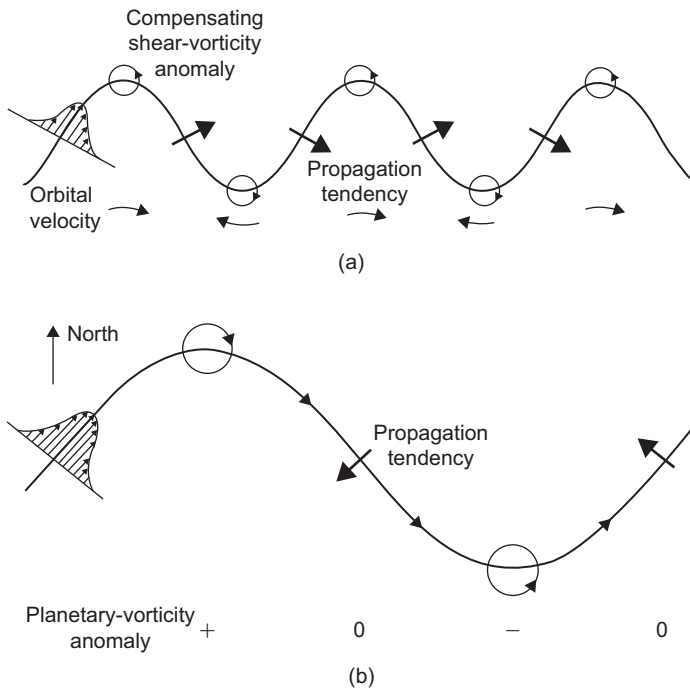


FIGURE 18.8 Schematic descriptions explaining why (a) curvature and (b) beta effects on an eastward jet induce meander-propagation tendencies that are, respectively, downstream and upstream.

vorticity considerations, as outlined previously. In the absence of the beta effect (or $\beta_0 Y \ll KU$), leftward and rightward turns create, respectively, clockwise and counterclockwise shear vorticity. Picturing these vorticity anomalies as vortices at the meanders' tips (Fig. 18.8a), we infer that the entrainment velocities at the inflection points between meanders all have a downstream component and that the meander pattern translates downstream. On a westerly jet, this direction is eastward. At the opposite extreme of a large beta effect and negligible curvature ($\beta_0 Y \gg KU$), the vorticity anomalies are cyclonic in troughs and anticyclonic in crests (Fig. 18.8b). The entrainment velocities at the inflection points all point westward. On a westerly jet, this is upstream. This mechanism is the same as that invoked in Section 9.4 to explain the westward phase propagation of planetary waves. (Compare Fig. 18.8b with Fig. 9.7)

We note, therefore, that curvature and beta effects induce opposite meander-propagation tendencies on an eastward jet. Comparing $\beta_0 Y$ with KU — or, equivalently, the wavelength to the critical meander scale — we conclude that if the former is larger than the latter, the meander propagates upstream (westward) and in the opposite direction otherwise. The meander is stationary if the tendencies cancel each other, which occurs if its wavelength is near the critical meander scale. Since this scale is rather long (220 km in the ocean and 1600 km

in the atmosphere, with $\beta_0 = 2 \times 10^{-11} \text{ m}^{-1} \text{ s}^{-1}$ and U ranging from 1 m/s to 50 m/s), observed meanders are usually of the curvature-type and propagate eastward.

18.1.3 Multiple Equilibria

Because the critical meander scale depends on the jet speed U , and also because the relation $\beta_0 Y \sim \mathcal{K}U$ depends on the shape of the meander (Y and \mathcal{K} are not simply related if the meander is other than sinusoidal), the critical size for meander stationarity depends on the jet speed and the meander shape. This conclusion is the basis of one explanation for the bimodality of the Kuroshio (Fig. 18.9). The geography of coastal Japan and the regional bottom topography force this intense current of the western North Pacific to pass through two channels, south of Yakushima Island (30°N, 130°E) and between Miyake and Hachijo Islands near the Izu Ridge (34°N, 140°E).

Between these two points, the current is known to assume one of two preferential states: a relatively straight path or a curved path with a substantial southward excursion. Each pattern persists for several years, whereas the transition from one to the other is relatively brief. The theory (Masuda, 1982; Robinson & Taft, 1972) explains this bimodal character by arguing that a stationary meander with a half-wavelength meeting the geographical specification may or may not exist, depending on the jet velocity. Calculations show that the meander state occurs if the jet velocity does not exceed a certain threshold value. At any velocity below this value, there exists a stationary-meander shape that meets the geographical constraints. At larger velocities, no stationary meander is possible, and the jet must assume a straight path.

The atmospheric analog of this oceanic situation is known as *blocking*, a word now used in a sense different from that used in Chapter 11. Here, blocking is a midlatitude phenomenon characterized by the unusual persistence of a nearly stationary meander on an eastward jet over topographic irregularities (Fig. 18.1). The theory (Charney & DeVore, 1979; Charney & Flierl, 1981) again invokes multiplicity of equilibrium solutions, including the normal state (no meander) and the anomalous blocking configuration (with large meander).

18.1.4 Stretching and Topographic Effects

Up to here, our considerations of vorticity adjustments in a jet meander included exchanges among planetary, shear, and orbital vorticity for an unchanged total. This is correct only for barotropic jets over a flat bottom, whereas in a baroclinic jet, in which vertical stretching can occur, potential vorticity rather than vorticity is the conserved quantity.

A complete theory involving all relevant dynamics such as momentum and mass balances is beyond our scope, and we derive here only the vertical-stretching tendency experienced by a fluid parcel in a meander. Assuming that the trade-off is solely between orbital vorticity due to the meander's curvature

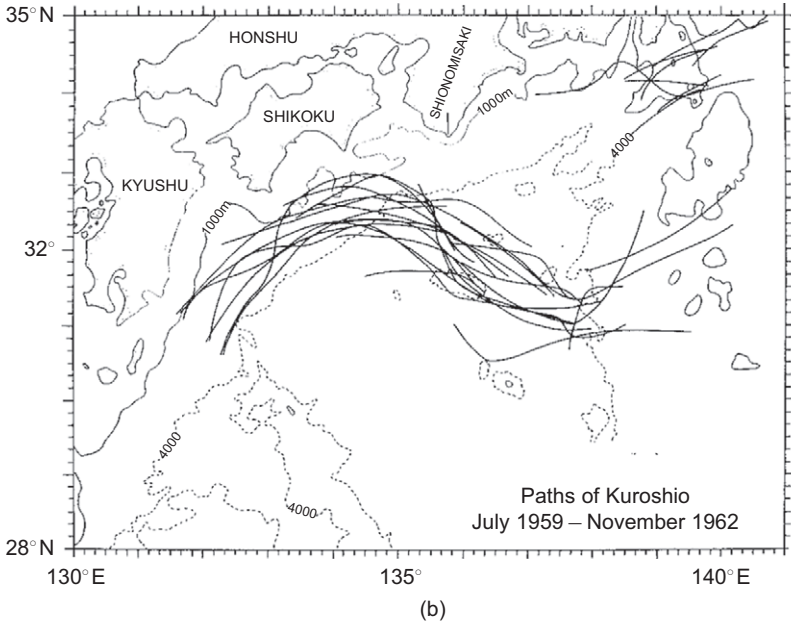
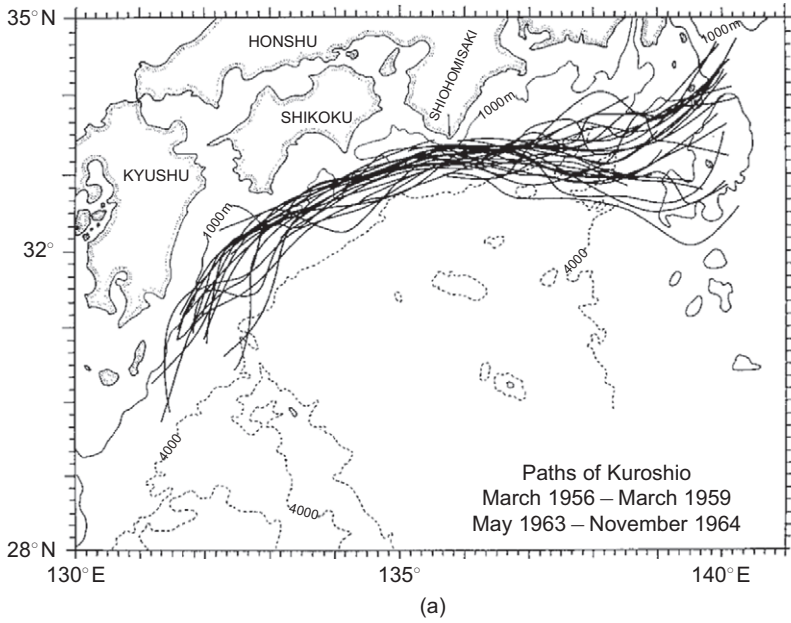


FIGURE 18.9 Observed Kuroshio paths: (a) straight jet and (b) stationary meander. (From Robinson & Taft, 1972)

and vertical stretching, we reason that a meander crest (with anticyclonic orbital vorticity) lowers the total vorticity and thus calls for a proportional decrease in the column's vertical thickness. In meander troughs, fluid columns are vertically stretched and shifted toward the anticyclonic side of the jet. In an oceanic surface jet such as the Gulf Stream, such a modification causes upwelling upon approaching crests and downwelling upon approaching troughs. Observations (Bower & Rossby, 1989) confirm such behavior, which can also be noted in numerical simulations (Fig. 18.10).

Just as meanders generate vertical stretching or squeezing, vertical stretching or squeezing induced by topography can cause meanders. To illustrate this, let us consider the case of a zonal jet (barotropic or baroclinic) on the beta plane that encounters a topographic step (Fig. 18.11). If the jet is flowing eastward (the usual situation) and enters a deeper region, the expansion in layer thickness translates first into a cyclonic deflection, away from the equator. As the Coriolis parameter increases away from the equator, this cyclonic vorticity is progressively exchanged downstream by a greater planetary vorticity, and the jet curvature weakens. Further poleward progression reverses the sense of orbital

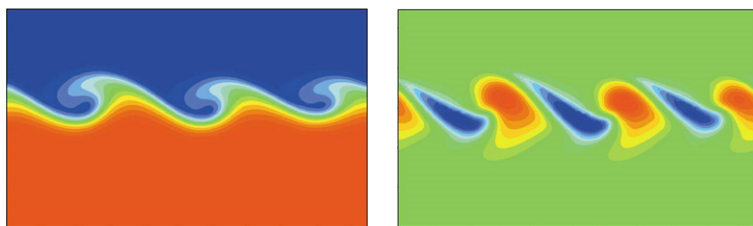


FIGURE 18.10 Frontal meander on a sea surface temperature field (left panel) and associated vertical-velocity distribution indicating upwelling and downwelling cells (right panel). Note that maxima of vertical velocity occur between the meander's crests and troughs (From Rixen, Beckers & Allen, 2001).

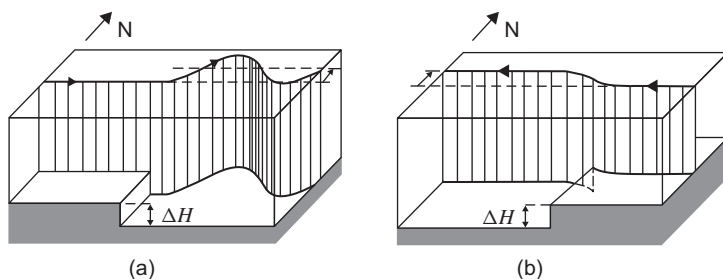


FIGURE 18.11 Eastward and westward jets passing over a topographic step: (a) the eastward jet develops an oscillatory behavior, whereas (b) the westward jet begins to feel the influence of the step upstream and executes a single meander. Both experience a net meridional shift $Y = f_0 \Delta H / \beta_0 h$, the sign of which depends on whether the step is up or down.

vorticity, and the jet oscillates back and forth about a new latitude (Fig. 18.11a). The average northward shift, Y , of the jet axis corresponds to an exchange between vertical stretching and increased planetary vorticity:

$$\frac{\beta_0 Y}{f_0} \sim \frac{\Delta H}{h}, \quad (18.10)$$

where ΔH is the height of the topographic step, and h is the upstream thickness of the jet. Because the first meander is rooted at the location of the step, the meander must be stationary, and therefore the wavelength must be comparable to the critical meander scale.

The same argument can be invoked for an eastward jet entering a shallower region to conclude that the flow exhibits a stationary oscillation about a net equatorward shift, given by Eq. (18.10) where ΔH is now negative. However, the argument fails for westward jets. Upon entering a deeper region, a fluid parcel acquires cyclonic vorticity and turns equatorward, its planetary vorticity decreases, further increasing the orbital vorticity. Clearly, if this were the case, the jet would be looping onto itself. Instead, the jet begins to be distorted ahead of the topographic step (Fig. 18.11b), acquiring an anticyclonic curvature in which the negative orbital vorticity is compensated by an increase in planetary vorticity. The jet thus reaches the step at an oblique angle. The nature of the vorticity adjustments past the step progressively restores the jet's original zonal orientation. A net meridional shift remains, expressing a balance between changes in planetary vorticity and vertical thickness. The reader can verify that this shift is again given by Eq. (18.10).

18.1.5 Instabilities

In addition to their propagation, meanders on a jet also distort and frequently grow, close onto themselves, and form eddies that separate from the rest of the jet. Such a finite change to the jet structure results from an instability, the nature of which is barotropic (Chapter 10), baroclinic (Chapter 17), or mixed. Barotropic instability proceeds with the extraction of kinetic energy from the horizontally sheared flow to feed the growing meander. The greater the shear in the jet, the more likely is this type of instability. Baroclinic instability, however, is associated with a conversion of available potential energy from the horizontal density distribution in balance with the thermal wind. Although the example treated in Section 10.4 suggests that critical wavelengths associated with barotropic instability scale as the jet width, consideration of baroclinic instability points to the critical role of the internal radius of deformation [see Eq. (17.48)]. If the two length scales are comparable, as is the case in a baroclinic jet with finite Rossby number, both processes may be equally active, and the instability is most likely of the mixed type (Griffiths, Killworth & Stern, 1982; Killworth, Paldor & Stern, 1984; Orlanski, 1968). The beta effect further complicates the situation, occasionally facilitating the eddy detachment process:

The large meridional displacement of the growing meander induces a westward-propagation tendency, whereas the high-curvature regions where the meander attaches to the rest of the jet induce a downstream propagation tendency. The result is a complex situation in which the outcome sensitively depends on the relative magnitudes of the different effects (Flierl, Malanotte-Rizzoli & Zabusky, 1987; Robinson, Spall & Pinardi, 1988). The meandering and eddy shedding of the Gulf Stream manifest this complexity.

The development of synoptic-scale weather disturbances, a process now called *cyclogenesis*, is thought to be initiated mostly by baroclinic instability, whereas accompanying finer-scale processes, such as cold and warm fronts, are explained by ageostrophic dynamics. The interested reader is referred to the book by Holton (1992) and Section 15.5.

18.2 VORTICES

A vortex, or eddy, is defined as a closed circulation that is relatively persistent. By persistence, we mean that the turnaround time of a fluid parcel embedded in the structure is much shorter than the time during which the structure remains identifiable. A *cyclone* is a vortex in which the rotary motion is in the same sense as the earth's rotation, counterclockwise in the northern hemisphere and clockwise in the southern hemisphere. An *anticyclone* rotates the other way, clockwise in the northern hemisphere and counterclockwise in the southern hemisphere.

The prototypical vortex is a steady circular motion on the f -plane. Using cylindrical coordinates, we can express the balance of forces in the radial direction r (measured outward) as follows:

$$-\frac{v^2}{r} - fv = -\frac{1}{\rho_0} \frac{\partial p}{\partial r}, \quad (18.11)$$

where v is the orbital velocity (positive counterclockwise), and p is the pressure (or Montgomery potential). Both v and p may be dependent upon the vertical coordinate, either height z or density ρ . This equation, called the *gradient-wind balance*, represents an equilibrium between three forces, the centrifugal force (first term), the Coriolis force (second term), and the pressure force (third term). Although the centrifugal force is always directed outward, the Coriolis and pressure forces can be directed either inward or outward, depending on the direction of the orbital flow and on the center pressure.

If we introduce the following scales, U for the orbital velocity, L for r (measuring the vortex radius), and ΔP for the pressure difference between the ambient value and that at the vortex center, we note that the terms composing (18.11) scale, respectively, as

$$\frac{U^2}{L}, \quad fU, \quad \frac{\Delta P}{\rho_0 L}. \quad (18.12)$$

At low Rossby numbers ($Ro = U/fL \ll 1$), the first term is negligible relative to the second (i.e., the centrifugal force is small compared with the Coriolis force), the balance is nearly geostrophic, providing

$$fU = \frac{\Delta P}{\rho_0 L}, \quad (18.13)$$

and thus $U = \Delta P/(\rho_0 f L)$. Since the pressure difference is most likely the result of a density anomaly $\Delta\rho$, the hydrostatic balance provides $\Delta P = \Delta\rho gH = \rho_0 g'H$, where H is the appropriate height scale (thickness of vortex), and $g' = g\Delta\rho/\rho_0$ is the reduced gravity. This leads to $U = g'H/fL$ and

$$Ro = \frac{U}{fL} = \frac{g'H}{f^2 L^2} = \left(\frac{R}{L}\right)^2, \quad (18.14)$$

in which we recognize the internal deformation radius $R = (g'H)^{1/2}/f$. Thus, a small Rossby number occurs as a consequence of a horizontal scale large compared with the deformation radius. This is typically the case in the largest weather cyclones and anticyclones at midlatitudes and in large-scale oceanic gyres (Fig. 18.12-top). Note that in this analysis, the Rossby number coincides with the Burger number. Thus, its smallness implies that the vorticity in broad gyres is mostly constrained by vertical stretching rather than relative vorticity (see Section 16.3). Also, the energy of such gyres is dominated by available potential energy rather than kinetic energy as shown by Eq. (16.34).

At scales on the order of the deformation radius, L can be taken equal to R , the Rossby number is on the order of unity, the velocity scale is $U = (g'H)^{1/2}$, and the centrifugal force is comparable with the Coriolis force. Around a low pressure, the outward centrifugal force partially balances the inward pressure force, leaving the Coriolis force to meet only the difference. By contrast, the Coriolis force acting on the flow around a high pressure must balance both the outward pressure force and the outward centrifugal force (Fig. 18.12-middle). Consequently, the orbital velocity in an anticyclone is greater than that in a cyclone of identical size and equivalent pressure anomaly. Tropical hurricanes (Anthes, 1982; Emmanuel, 1991) and the so-called rings shed by the Gulf Stream (Flierl, 1987; Olson, 1991) fall in the category of vortices with length scale on the order of the deformation radius.

At progressively shorter radii, the centrifugal force becomes increasingly important, and for $L \ll R$, the Coriolis force becomes negligible. The cyclone-anticyclone nomenclature then loses its meaning, and the relevant characteristic is the sign of the pressure anomaly. The inward force around a low pressure is balanced by the outward centrifugal force regardless of the direction of rotation (Fig. 18.12-bottom). Such a state is said to be in *cyclostrophic balance*. Examples are tornadoes and bathtub vortices. A vortex with high-pressure center cannot exist because pressure and centrifugal forces would both be directed outward.

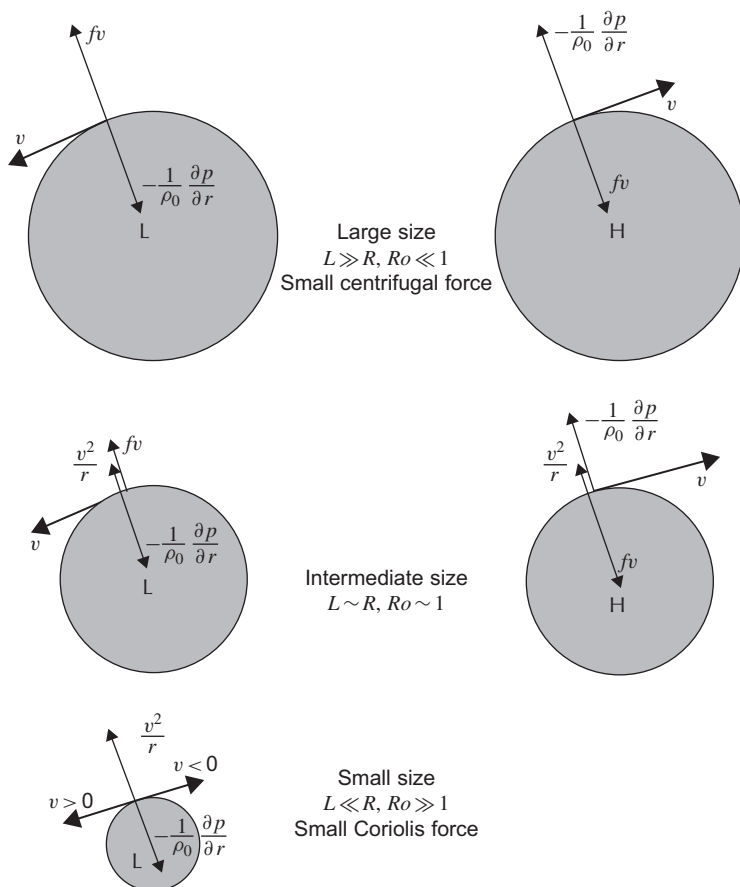


FIGURE 18.12 Balances between pressure gradient $-(1/\rho_0)\partial p/\partial r$, Coriolis fv , and centrifugal v^2/r forces in northern hemispheric circular vortices. The letters L and H indicate low and high pressures, respectively.

It is interesting to determine the minimum size for which an anticyclone of given pressure anomaly can exist. Returning to the gradient-wind balance where we introduce $v = -fr/2 + v'$, we write

$$\frac{f^2 r}{4} + \frac{1}{\rho_0} \frac{\partial p}{\partial r} = \frac{1}{r} v'^2 \geq 0. \quad (18.15)$$

Integrating over the radius a of the vortex and defining the pressure anomaly $\Delta p = p(r=0) - p(r=a)$, we obtain

$$a^2 \geq \frac{8\Delta p}{\rho_0 f^2}. \quad (18.16)$$

For a low-pressure center ($\Delta p < 0$), this inequality yields no constraint, whereas for a high-pressure center ($\Delta p > 0$), it specifies a minimum vortex radius. Below this minimum, high-pressure centers simply do not exist as isolated steady structures.

Let us now examine how an existing vortex can move within the fluid that surrounds it. To do this, we consider a vortex contained within a single layer of fluid, be it the lowest, the uppermost, or any intermediate layer in the fluid. If the local thickness of this layer is h , and the pressure (actually, Montgomery potential) is p , we write, in density coordinates,

$$\frac{\partial u}{\partial t} + u \frac{\partial u}{\partial x} + v \frac{\partial u}{\partial y} - f v = -\frac{1}{\rho_0} \frac{\partial p}{\partial x}, \quad (18.17a)$$

$$\frac{\partial v}{\partial t} + u \frac{\partial v}{\partial x} + v \frac{\partial v}{\partial y} + f u = -\frac{1}{\rho_0} \frac{\partial p}{\partial y}, \quad (18.17b)$$

$$\frac{\partial h}{\partial t} + \frac{\partial}{\partial x}(hu) + \frac{\partial}{\partial y}(hv) = 0. \quad (18.17c)$$

We further restrict ourselves to the f -plane. At large distances from the vortex center, in what can be considered the ambient fluid, we assume that there exists a steady uniform flow (\bar{u} , \bar{v}) and a uniform thickness gradient ($\partial \bar{h}/\partial x$, $\partial \bar{h}/\partial y$). According to Eqs. (18.17a) and (18.17b), this flow must be geostrophic, and according to Eq. (18.17c), it must be aligned with the direction of constant layer thickness:

$$-f \bar{v} = -\frac{1}{\rho_0} \frac{\partial \bar{p}}{\partial x}, \quad (18.18a)$$

$$+f \bar{u} = -\frac{1}{\rho_0} \frac{\partial \bar{p}}{\partial y}, \quad (18.18b)$$

$$\bar{u} \frac{\partial \bar{h}}{\partial x} + \bar{v} \frac{\partial \bar{h}}{\partial y} = 0. \quad (18.18c)$$

A thickness gradient is retained because, in some instances, a thermal wind in layers above or below may be accompanied by such a thickness variation. Also, if the vortex lies in the lowest layer, the thickness gradient may represent a bottom slope. The assumption of uniformity of \bar{u} , \bar{v} , and of the derivatives of \bar{p} and \bar{h} is justified if the ambient-flow properties vary over horizontal distances much longer than the vortex diameter. Defining the velocity components, pressure, and layer-thickness variations proper to the vortex as $u' = u - \bar{u}$, $v' = v - \bar{v}$, $p' = p - \bar{p}$, and $h' = h - \bar{h}$, we can transform Eqs. (18.17) as follows:

$$\frac{\partial u'}{\partial t} + (\bar{u} + u') \frac{\partial u'}{\partial x} + (\bar{v} + v') \frac{\partial u'}{\partial y} - f v' = -\frac{1}{\rho_0} \frac{\partial p'}{\partial x} \quad (18.19a)$$

$$\frac{\partial v'}{\partial t} + (\bar{u} + u') \frac{\partial v'}{\partial x} + (\bar{v} + v') \frac{\partial v'}{\partial y} + f u' = -\frac{1}{\rho_0} \frac{\partial p'}{\partial y} \quad (18.19b)$$

$$\frac{\partial h'}{\partial t} + \frac{\partial(h'\bar{u})}{\partial x} + \frac{\partial(h'\bar{v})}{\partial y} + \frac{\partial}{\partial x}[(\bar{h} + h')u'] + \frac{\partial}{\partial y}[(\bar{h} + h')v'] = 0. \quad (18.19c)$$

We then define the anomalous layer volume due to the vortex:

$$V = \iint h' dx dy, \quad (18.20)$$

where the integration covers the entire horizontal extent of the layer. The perturbation h' induced by the vortex is assumed to be sufficiently localized to make the preceding integral finite. The use of continuity [equation \(18.19c\)](#) followed by integration by parts over several terms shows that the temporal derivative of this volume,

$$\frac{dV}{dt} = \iint \frac{\partial h'}{\partial t} dx dy \quad (18.21)$$

vanishes, as we expect. Defining the coordinates of the vortex position by the volume-weighted averages

$$X = \frac{1}{V} \iint x h' dx dy, \quad Y = \frac{1}{V} \iint y h' dx dy, \quad (18.22)$$

we can track the vortex displacements by calculating their temporal derivatives. For X , we obtain successively

$$\begin{aligned} \frac{dX}{dt} &= \frac{1}{V} \iint x \frac{\partial h'}{\partial t} dx dy \\ &= \frac{-1}{V} \iint \left\{ x \bar{u} \frac{\partial h'}{\partial x} + x \bar{v} \frac{\partial h'}{\partial y} + x \frac{\partial}{\partial x}[(\bar{h} + h')u'] + x \frac{\partial}{\partial y}[(\bar{h} + h')v'] \right\} dx dy \\ &= \frac{+1}{V} \iint [\bar{u} h' + (\bar{h} + h')u'] dx dy \\ &= \bar{u} + \frac{1}{V} \iint h u' dx dy. \end{aligned} \quad (18.23)$$

Similarly, we obtain for the other coordinate

$$\frac{dY}{dt} = \bar{v} + \frac{1}{V} \iint h v' dx dy. \quad (18.24)$$

The preceding integrals cannot be evaluated without knowing the precise structure of the vortex. However, a second time derivative will bring forth the acceleration ($\partial u'/\partial t$, $\partial v'/\partial t$), which is provided by the equations of motion,

(18.19a) and (18.19b). For the X -coordinate, we obtain

$$\begin{aligned}\frac{d^2X}{dt^2} &= \frac{1}{V} \iint \left[\frac{\partial h'}{\partial t} u' + (\bar{h} + h') \frac{\partial u'}{\partial t} \right] dx dy \\ &= \frac{-1}{V} \iint \left[\frac{\partial}{\partial x} (huu') + \frac{\partial}{\partial y} (hvu') \right] dx dy \\ &\quad + \frac{f}{V} \iint hv' dx dy - \frac{1}{\rho_0 V} \iint h \frac{\partial p'}{\partial x} dx dy.\end{aligned}\quad (18.25)$$

The pressure anomaly p' associated with the vortex motions can be related by hydrostatic balance to the layer-thickness anomaly. If other layers do not move and keep their pressure value over time, the pressure anomaly inside the vortex is given by integration of Eq. (12.14) where the pressure anomaly above the layer of interest is zero:

$$p' = \rho_0 g' h', \quad (18.26)$$

with a suitable definition of the reduced gravity g' . Note that if the vortex is contained in the lowest layer above an uneven bottom, the bottom elevation does not enter (18.26) but instead enters the corresponding hydrostatic balance for the mean-flow properties.

Noting that the first integral in Eq. (18.25) vanishes because u' and v' go to zero at large distances from the vortex, that the second integral can be eliminated by use of Eq. (18.24), and that the third integral, integrated by parts, can be simplified with use of Eq. (18.26), we obtain

$$\frac{d^2X}{dt^2} = f \frac{dY}{dt} - f \bar{v} + g' \frac{\partial \bar{h}}{\partial x}. \quad (18.27)$$

A similar treatment of the second derivative of Y yields

$$\frac{d^2Y}{dt^2} = -f \frac{dX}{dt} + f \bar{u} + g' \frac{\partial \bar{h}}{\partial y}. \quad (18.28)$$

Because the gradient of \bar{h} is assumed uniform, and f , \bar{u} , and \bar{v} are constants, the preceding two equations can be solved for the velocity of the vortex:

$$\frac{dX}{dt} = \left(\bar{u} + \frac{g'}{f} \frac{\partial \bar{h}}{\partial y} \right) (1 - \cos ft) - \left(\bar{v} - \frac{g'}{f} \frac{\partial \bar{h}}{\partial x} \right) \sin ft \quad (18.29a)$$

$$\frac{dY}{dt} = \left(\bar{v} - \frac{g'}{f} \frac{\partial \bar{h}}{\partial x} \right) (1 - \cos ft) + \left(\bar{u} + \frac{g'}{f} \frac{\partial \bar{h}}{\partial y} \right) \sin ft, \quad (18.29b)$$

where the constants of integration have been determined under the assumption that the vortex is not translating initially. In the preceding solution, we

recognize inertial oscillations superimposed on a mean drift. This mean drift has two components:

$$c_x = \bar{u} + \frac{g'}{f} \frac{\partial \bar{h}}{\partial y}, \quad c_y = \bar{v} - \frac{g'}{f} \frac{\partial \bar{h}}{\partial x}. \quad (18.30)$$

The first contribution (\bar{u}, \bar{v}) indicates that the vortex is entrained by the ambient motion of its containing layer. Together, this entrainment and the inertial oscillations do not distinguish the vortex from a single fluid parcel. The cause of the second contribution, proportional to the gradient of \bar{h} , is less obvious and is what really distinguishes a vortex from a fluid parcel.

The existence of a thickness gradient in the vicinity of the vortex implies a nonuniform distribution of potential vorticity, which the swirling motion of the vortex redistributes; fluid parcels on the edge of the vortex are thus stretched and squeezed and develop vorticity anomalies that, in turn, act to displace the main part of the vortex. As the example in Fig. 18.13 illustrates, a northward decrease of layer thickness in the northern hemisphere causes squeezing on parcels moved northward and stretching on those moved southward. (The sense of rotation in the vortex is irrelevant here.) This causes the fluid on the northern flank of the vortex to acquire anticyclonic vorticity and that on the southern flank to acquire cyclonic vorticity. Both vorticity anomalies induce a westward displacement of the bulk of the vortex. Equations (18.30) confirm that those conditions ($\partial \bar{h}/\partial x = 0$, $\partial \bar{h}/\partial y < 0$, $f > 0$) imply a negative c_x and a zero c_y . The general rule is that the vortex translates with the thin-layer side on its right in the northern hemisphere and on its left in the southern hemisphere.

Gradients in the vortex-containing layer can be caused by one of two reasons. If other layers, above or below, flow at speeds different from that of the vortex layer, there exists a thermal wind, which by virtue of the Margules

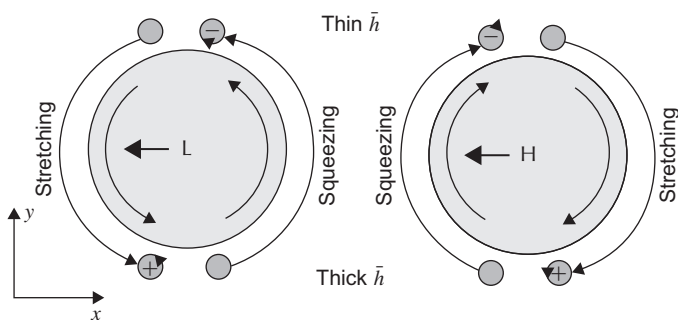


FIGURE 18.13 Lateral drift of a vortex embedded in layer of varying thickness. Advection by surrounding fluid induces cyclonic and anticyclonic vorticities, which combine to induce a drift of the vortex along lines of constant thickness. In the northern hemisphere (as drawn in the figure), the vortex moves with the thin-layer side on its right. Direction is opposite in the southern hemisphere.

relation [see (15.5)] requires sloping density surfaces and, therefore, varying layer thicknesses. It is left to the reader to show that in such a case the vorticity-induction mechanism described in the preceding paragraph amounts to a drift of the vortex in the same direction as the thermal wind. The other reason for layer-thickness variations is bottom topography. If the vortex is contained in the lower layer, bounded below by a sloping bottom, fluid parcels surrounding the vortex will be moved up or down this slope and undergo vorticity adjustments. The result (see Fig. 18.13 again) is a drift of the vortex with the shallower region to its right in the northern hemisphere and to its left in the southern hemisphere. Nof (1983) discusses this effect for cold eddy lenses on the ocean bottom.

Note that if the vortex starts from a resting position, its migration is not immediately transverse to the thickness gradient but is up-gradient, as solution (18.29) indicates for small values of time. In the case of a sloping bottom, this implies that the vortex first goes downhill, gradually acquiring a velocity in that direction, and under the action of the Coriolis force has its trajectory subsequently deflected in the direction transverse to the topographic gradient. (Compare this situation with that of Analytical Problem 2.9.)

Because of the analogy between a topographic slope and the beta effect (see Section 9.6), the preceding conclusions can be extrapolated to the motion of vortices on the beta plane. Regardless of their polarity (cyclonic or anticyclonic), vortices have a self-induced westward tendency. Repeating the argument made with Fig. 18.13, with the replacement of the thick-to-thin direction by the northward direction, we conclude that surrounding parcels entrained from the southern tip to the northern end acquire planetary vorticity and thus develop anticyclonic relative vorticity. Similarly, the surrounding parcels entrained from north to south develop cyclonic relative vorticity. The combined effect at the latitude of the vortex center is a westward drift. Theories (Cushman-Roisin, Chassignet & Tang, 1990 and references therein) show that the induced speed is on the order of $\beta_0 R^2$, where R is the internal radius of deformation, being slightly larger for anticyclones than cyclones. However, in both atmosphere and oceans, this speed is usually too weak to be noticeable compared with the entrainment by the ambient flow.

Instead of interpreting the westward drift in terms of potential vorticity, we can also explain the drift by a balance of forces. On the northern side of an anticyclonic eddy in the northern hemisphere, geostrophic velocity is smaller than on the southern side under identical Coriolis force balancing the pressure gradient (Fig. 18.14). The velocity difference yields a convergence (divergence) on the western (eastern) flank of the vortex. This in turn causes a vertical displacement of the density interface, causing the vortex volume to slide sideways with upwelling in its eastern flank and downwelling on its western flank. For the cyclone, similar reasoning yields again a westward displacement.

Implicit in the preceding derivations was the assumption that all variables related to the vortex decay sufficiently fast away from the vortex core to make all integrals finite. However, in the presence of a potential-vorticity gradient

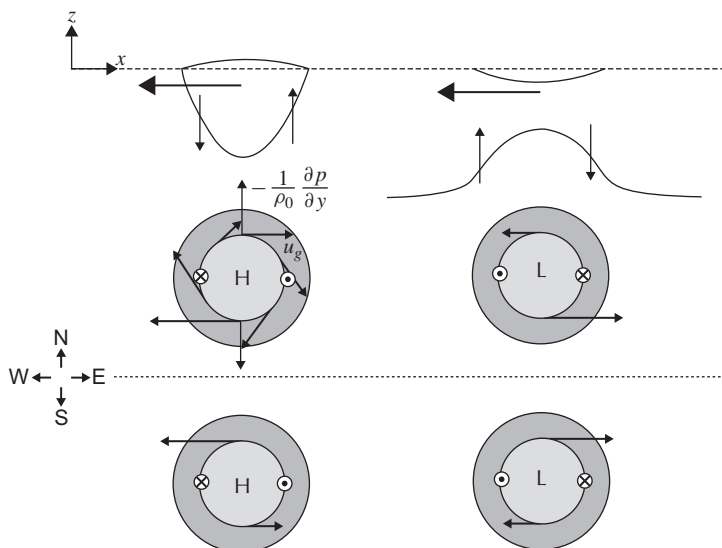


FIGURE 18.14 Alternative explication of the westward drift for an anticyclone (left side) and cyclone (right side). The vertical section at top shows an anticyclone's core of lighter fluid (top-left) and the reduced layer thickness associated with a cyclone (top-right). The plots below represent top views spanning the equator (dotted line) and show the velocity fields. The convergence and divergence pattern associated with north-south velocity differences cause the vortex to move westward regardless of its sense of rotation.

such as one created by a layer-thickness gradient (see the preceding text) or by the beta effect ($\beta_0 = df/dy$), waves are possible (Sections 9.4 and 9.5) and energy can be radiated away to large distances from the vortex, yielding non negligible eddy-related motions there. As it turns out, it is possible to predict, at least qualitatively, the effect of such waves by considering the early time evolution of the vortex. Figure 18.15 depicts the relative-vorticity adjustments brought to surrounding fluid parcels as they are moved by the vortex for the first quarter of their evolution. As for linear waves (Section 9.6), there is a direct analogy between the layer-thickness gradient and the beta effect: The thin-layer side and the poleward direction are dynamically similar, for they both point to an increase in potential vorticity. After a quarter turn, parcels surrounding the vortex acquire relative vorticity by stretching (or squeezing) or a decrease (or increase) in planetary vorticity. As Fig. 18.15 reveals, the cumulative effect in the northern hemisphere is a migration of cyclones toward decreasing layer thicknesses or northward; anticyclones migrate in the opposite direction. As vortices move in those directions, their own core fluid undergoes similar stretching or squeezing or planetary-vorticity changes. In all cases, the net result is a decrease in the absolute value of the relative vorticity and thus an overall spin-down of the vortex.

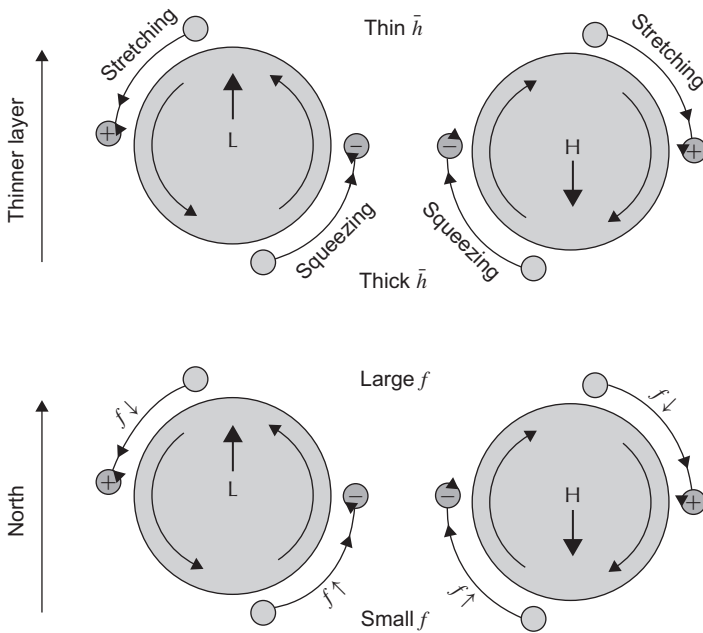


FIGURE 18.15 Secondary drift of vortices. The advection of surrounding fluid induces cyclonic and anticyclonic vortices on the flanks of the vortex, which combine to cause a drift as indicated. This drift component is perpendicular and in addition to that depicted in Fig. 18.13. Again, the figure is drawn for the northern hemisphere. In the southern hemisphere, cyclones still move in the direction of smaller layer thickness or poleward, and anticyclones move in the direction of greater layer thickness, or equatorward.

In the study of hurricane motion, Shapiro (1992) distinctly shows how the trajectory of the hurricane center (a low-pressure center and thus a cyclone) can be explained by the mechanisms just summarized. Here, the beta effect is relatively unimportant, but the presence of a westerly wind aloft and its accompanying layer-thickness gradient (thicker southward) combine to make the hurricane progress in the northwestward direction.

A discussion of geophysical vortices ought to address additional aspects such as axisymmetrization (assuming a nearly circular shape despite anisotropic birthing conditions), instabilities, secondary motions, frictional spin-down, wave radiation, and so on. Partly, because space does not permit a deeper discussion here but mostly because these aspects tend to be quite different in the atmosphere and ocean, the reader interested in atmospheric vortices is referred to the monograph by Anthes (1982), and the reader interested in oceanic vortices is referred to the book edited by Robinson (1983). Laboratory simulations of geophysical vortices have also been conducted; an interesting article on vortex instabilities is that by Griffiths and Linden (1981).

18.3 GEOSTROPHIC TURBULENCE

We alluded to geostrophic turbulence, which is the study of a large number of interacting vortices, in Section 16.6 when we introduced nonlinear effects in quasi-geostrophic dynamics. Here, we tackle the subject from the vortex point of view, without making the quasi-geostrophic assumption.

When several eddies are present and not too distant from one another, interactions are unavoidable. Vortices shear and peel off the sides of their neighbors and, at times, merge to create larger vortices. The sheared elements either curl onto themselves, forming new, smaller vortices, or dissipate under the action of friction. The net result is a combination of consolidation and destruction. When many vortices are simultaneously present, the situation is best described in a statistical sense.

A number of important properties can be derived rather simply by considering three integrals of motion, namely, the kinetic energy, the available potential energy, and the *enstrophy*, the latter being the integrated squared vorticity. We thus define the following:

$$\text{Kinetic energy: } KE = \frac{1}{2} \rho_0 \iiint (u^2 + v^2) dx dy dz \quad (18.31a)$$

$$\text{Available potential energy: } APE = \frac{1}{2} \rho_0 \iiint N^2 h^2 dx dy dz \quad (18.31b)$$

$$\text{Enstrophy: } S = \frac{1}{2} \iiint \left(\frac{\partial v}{\partial x} - \frac{\partial u}{\partial y} \right)^2 dx dy dz. \quad (18.31c)$$

In the formulation of the kinetic energy, the contribution of vertical velocity is usually insignificant. (It is insignificant whenever hydrostatic balance holds.) If the horizontal velocity scale is U , the domain depth is H , and the horizontal area is A , the size of KE is about $\rho_0 U^2 HA$. Available potential energy was defined in Eq. (16.29). If the vertical displacements of the density surfaces scale as ΔH ($\Delta H \leq H$, naturally) and if reduced gravity is introduced via $g' = N^2 H$ [see (18.2)], the available potential energy is on the order of $\rho_0 g' \Delta H^2 A$. For eddies of average size L , vorticity scales as U/L and enstrophy as $(U/L)^2 HA$. Finally, if we invoke geostrophy to set the velocity scale, we state $f_0 U \sim g' \Delta H / L$ (barring a substantial barotropic component) and write

$$KE \sim \rho_0 \left(\frac{g' \Delta H}{f_0 L} \right)^2 HA \quad (18.32a)$$

$$APE \sim \rho_0 g' \Delta H^2 A \quad (18.32b)$$

$$S \sim \left(\frac{g' \Delta H}{f_0 L^2} \right)^2 HA. \quad (18.32c)$$

The ratio of kinetic to potential energy is

$$\frac{KE}{APE} \sim \frac{g'H}{f_0^2 L^2} = \left(\frac{R}{L}\right)^2, \quad (18.33)$$

where R is the internal radius of deformation. We recognize here the Burger number of Eq. (16.34).

As the interactions among vortices proceed, the shearing and tearing of vortices introduce motions at ever shorter scales, until frictional dissipation becomes important. Because S increases much faster than KE with decreasing length scales, while APE is unaffected, friction removes disproportionately more enstrophy than kinetic energy and, surely, potential energy. In first approximation, we can assume that the total energy is conserved, while enstrophy decays with time. In a fixed domain ($HA = \text{constant}$) and with constant f_0 and g' values (no heating or cooling), a decrease in enstrophy requires, by virtue of (18.32c), a decrease in the ratio $\Delta H/L^2$.

At short length scales ($L \ll R$), the energy consists primarily of kinetic energy, via (18.33), and its near conservation requires that $\Delta H/L$ remain approximately constant. The only possibility that satisfies both requirements is a steady increase of the length scale L , with a proportional increase in eddy amplitude ΔH . Thus, vortices become, on average, larger and stronger. Obviously, to conserve the total space allowed to them, they also become fewer. There is thus a natural tendency toward successive eddy mergers. With every merger, energy is consolidated into larger structures with concomitant enstrophy losses. Thus, the eddy field gradually assumes a dual pattern with ever fewer and larger vortices (coherent structures of increasing length scale) swimming in an increasingly sheared and disordered interstitial fluid (incoherent flow of decreasing length scale).

As the length scale of vortices increases toward the radius of deformation, the relative importance of potential energy increases. Because APE increases like ΔH^2 , further increase in mean eddy amplitude ΔH requires a corresponding decrease in kinetic energy to preserve total energy, and $\Delta H^2/L^2$ must begin to decrease. The result is that ΔH and L continue to increase but no longer proportionally, L increasing faster than ΔH .

As the length scale continues to increase, indicating continued merging activity, it will eventually become much larger than R . Then, the energy is primarily in the form of potential energy, and its conservation requires a saturated value of ΔH . Further enstrophy decrease under frictional action is possible only with a further increase in length scale L (Rhines, 1975; Salmon, 1982). In sum, the interactions of a large number of vortices without addition of energy lead to an irreversible tendency toward fewer and larger vortices. This implies an emergence of coherent structures from a random initial vorticity field. As for the mean eddy amplitude, it increases only up to a certain point. The maximum possible eddy amplitude is achieved when almost all the energy available is in

the form of available potential energy—that is,

$$\Delta H_{\max} \sim \sqrt{\frac{E}{\rho_0 g' A}}, \quad (18.34)$$

where E is the total energy present in the system ($E = KE + APE$), and A is the horizontal area of the system. Should this value exceeds the depth H of the domain, vortex amplitudes will be limited by the latter and not all the energy can be turned into potential energy; a certain portion of the energy must remain in the form of kinetic energy, implying a limit to the length scale L .

Pioneering results concerning the emergence of coherent vortices in quasi-geostrophic turbulence can be found in McWilliams (1984, 1989). Let us also note that the tendency toward successive merger is at the basis of the theories (Galperin, Nakano, Huang & Sukoriansky, 2004; Williams and Wilson, 1988, and references therein) that explain the persistence of the Great Red Spot in Jupiter's atmosphere (Fig. 1.5). This begs the question as to why no single dominating vortex occurs in our terrestrial atmosphere as on Jupiter. The answer lies in diabatic and orographic effects constantly acting to form and destroy existing atmospheric vortices. In other words, geostrophic turbulence in the earth's atmosphere is never freely evolving for very long. Similarly, wind forcing over the ocean and dissipation by internal waves and in coastal areas combine to prevent oceanic geostrophic turbulence from following its intrinsic evolution.

18.4 SIMULATIONS OF GEOSTROPHIC TURBULENCE

In the study of many interacting eddies and the statistical analysis of geostrophic turbulence, lateral boundaries are not the focus of the investigation, and may be ignored by invoking periodicity in space (as if the same domain were repeating itself in the several directions of space). When this is the case, a particular *meshless* spectral method can be used for numerical simulations. We already encountered a spectral technique for the solution of linear problems (see Section 8.8), and we now adapt it to a nonlinear problem.

For simplicity, we design the numerical scheme for a one-layer quasi-geostrophic system with rigid-lid and scale-selective biharmonic dissipation of vorticity (see Section 10.6 on filtering). The governing equations on the f -plane are thus

$$\frac{\partial q}{\partial t} + J(\psi, q) = -\mathcal{B} \left(\frac{\partial^4 q}{\partial x^4} + 2 \frac{\partial^4 q}{\partial x^2 \partial y^2} + \frac{\partial^4 q}{\partial y^4} \right) \quad (18.35a)$$

$$\frac{\partial^2 \psi}{\partial x^2} + \frac{\partial^2 \psi}{\partial y^2} = q \quad (18.35b)$$

where the parameter \mathcal{B} controls the strength of the damping. Both stream-function ψ and potential vorticity q are expanded as truncated series of sine and cosine functions spanning the periodic domain of interest $0 \leq x \leq L_x$ and

$0 \leq y \leq L_y$. For convenience, we use complex exponentials instead of sine and cosine functions and write

$$\tilde{\psi}(x, y, t) = \sum_k \sum_l \Psi_{kl}(t) e^{i \frac{2\pi kx}{L_x}} e^{i \frac{2\pi ly}{L_y}}, \quad (18.36a)$$

$$\tilde{q}(x, y, t) = \sum_k \sum_l Q_{kl}(t) e^{i \frac{2\pi kx}{L_x}} e^{i \frac{2\pi ly}{L_y}}. \quad (18.36b)$$

The time-dependent coefficients Ψ_{kl} and Q_{kl} , also called *spectral coefficients*, are the amplitudes of the spatial Fourier modes, and their value over time constitutes the solution to the problem. We obtain equations governing their evolution by multiplying (18.35) by $\exp(-2i\pi k'x/L_x) \exp(-2i\pi l'y/L_y)$ and integrating over the extent of the domain. The orthogonality of the sine and cosine functions then isolates the time evolution of $Q_{k'l'}$ and, after relabeling k' as k and l' as l , leads to

$$\frac{\partial Q_{kl}}{\partial t} + \frac{1}{L_x L_y} \int_0^{L_x} \int_0^{L_y} J(\tilde{\psi}, \tilde{q}) e^{-i \frac{2\pi kx}{L_x}} e^{-i \frac{2\pi ly}{L_y}} dy dx = -\alpha_{kl} Q_{kl} \quad (18.37)$$

with

$$\alpha_{kl} = \mathcal{B} \left[\left(\frac{2\pi k}{L_x} \right)^2 + \left(\frac{2\pi l}{L_y} \right)^2 \right]^2. \quad (18.38)$$

Note how the dissipation term involving derivatives was nicely transformed into an algebraic operation and how clearly the attenuation of amplitudes for different wavelengths can be seen in the value of α_{kl} .

Applying the same spectral projection to Eq. (18.35b) that serves as the definition of potential vorticity, we obtain the governing equation for streamfunction amplitudes:

$$-\left[\left(\frac{2\pi k}{L_x} \right)^2 + \left(\frac{2\pi l}{L_y} \right)^2 \right] \Psi_{kl} = Q_{kl}. \quad (18.39)$$

The solution of what was the Poisson equation is now trivial since the equation is now algebraic and retrieving the streamfunction from vorticity is reduced to a division. Note that for wavenumber $k=l=0$, there is no need for a division by zero, because the streamfunction is defined up to an arbitrary constant Ψ_{00} , which plays no role in the dynamics. All linear operations are trivial to perform in the so-called *spectral space*, i.e., in the discrete (k, l) space associated with wavelengths L_x/k and L_y/l . Also, initialization of the fields from a given streamfunction in physical space can easily be translated into initial conditions for the spectral coefficients. Because periodic boundary conditions are already taken into account by the use of periodic functions in the truncated series, all we have

to do is to calculate the time evolution of the amplitudes using Eq. (18.37). Once amplitudes are known, series (18.36) can be evaluated at any desired location (x, y) to obtain the solution in physical space.

There remains, however, to calculate the contribution from the nonlinear Jacobian term that appears inside the integral term of Eq. (18.37). Each derivative appearing in this term can be evaluated by means of the derivatives of the basis functions, for example

$$\begin{aligned}\frac{\partial \tilde{\psi}}{\partial x} &= \sum_k \sum_l a_{kl} e^{i \frac{2\pi kx}{L_x}} e^{i \frac{2\pi ly}{L_y}} \\ a_{kl} &= i \frac{2\pi k}{L_x} \Psi_{kl}\end{aligned}\quad (18.40)$$

and similarly for the other derivatives $\partial \tilde{\psi}/\partial y$, $\partial \tilde{q}/\partial x$, and $\partial \tilde{q}/\partial y$. The Jacobian term can then be expressed from products of these series-expansions and becomes

$$J(\tilde{\psi}, \tilde{q}) = \frac{4\pi^2}{L_x L_y} \sum_i \sum_j \sum_m \sum_n (jm - in) \Psi_{ij} \mathcal{Q}_{mn} e^{i \frac{2\pi(i+m)x}{L_x}} e^{i \frac{2\pi(j+n)y}{L_y}}. \quad (18.41)$$

Then, because of the orthogonality property of the basis functions, most of those terms after projection onto the (k, l) component in Eq. (18.37) vanish, except the terms for which $i + m = k$ and $j + n = l$. Using Eq. (18.39) to eliminate the streamfunction amplitudes and introducing the so-called interaction coefficients c_{mnkl} , we finally arrive at the equations governing the temporal evolution of the spectral coefficients of potential vorticity:

$$\frac{\partial \mathcal{Q}_{kl}}{\partial t} = -\alpha_{kl} \mathcal{Q}_{kl} - \sum_m \sum_n c_{mnkl} \mathcal{Q}_{mn} \mathcal{Q}_{k-m, l-n}. \quad (18.42)$$

For the time stepping of \mathcal{Q}_{kl} , any previous numerical method may be used since the interaction coefficients c_{mnkl} are known as well as parameters α_{kl} , which depend on the particular form of physical dissipation utilized in the model. The nonlinear term clearly reflects the physical interaction between wave components (eddies) at different scales.

The method has the advantage of automatically including periodic boundary conditions and avoiding the inversion of a Poisson equation at every time step. It further avoids another problem that can plague nonlinear numerical models, namely the aliasing of higher, unresolved wavenumbers created by interactions into lower, resolved wavenumbers (see Section 1.12 and 10.5). As we work in spectral space, we can easily disregard the higher wavenumbers that are created by nonlinear combinations by setting the corresponding interaction coefficients to zero.

The method is thus appealing but has a major drawback, its computational cost. If we retain N Fourier coefficients for each spatial direction, each sum in

Eq. (18.42) involves N terms, and a double sum requires N^2 operations. For each of the N^2 equations for Fourier amplitudes, we must therefore perform N^2 operations for the sums associated with the nonlinear term. The computational burden is then proportional to N^4 (M^2 in terms of the number M of unknowns). Because one aim of a geostrophic turbulence model is the study of turbulence per se, unrealistic subgrid-scale parameterizations must be avoided, and very high spatial resolution must be attempted. The computational cost of the present approach can rapidly become prohibitive.

A major breakthrough for the spectral approach came with the discovery of the so-called *Transform Method* (e.g., Orszag, 1970). The basic idea is to switch back and forth between physical space and spectral space, performing each task in the space in which it is least burdensome. Thus, one first calculates derivatives in spectral space by generating coefficients as in Eq. (18.40). The spatial derivative can then be calculated at any location from the Fourier series, on a regular grid spanning the physical domain of interest. Once all derivatives appearing in the Jacobian have been so calculated, the latter can be calculated in physical space from products at each grid node. With the numerical value of the Jacobian known on a regular grid, its spectral amplitudes are then obtained in the wavenumber space, which permit the calculation of time changes of the spectral coefficient of vorticity (Fig. 18.16). Because in the physical domain, the cost of operations associated with the Jacobian is only proportional to the number of grid points M , there is a net gain from the detour if the cost of the transformation falls below M^2 .

For such method to be viable, the number of calculations involved in the switch back and forth between physical domain and spectral space must be lower than the number of calculations saved by performing the tasks in their respective space of greatest ease. This is the case because there exists a fast transformation method to pass back and forth between physical domain and spectral space.

For a one-dimensional case, the Fourier transformation can be achieved efficiently by the so-called Fast Fourier Transform (FFT, see Appendix C), which

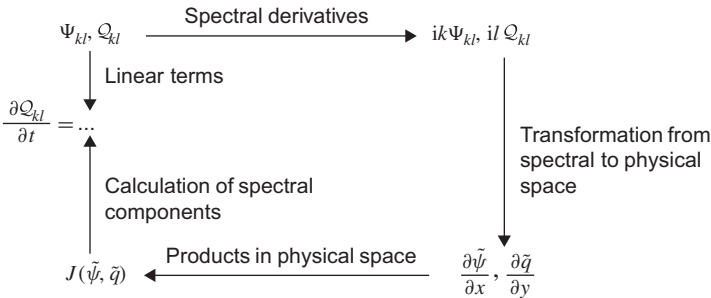


FIGURE 18.16 Schematic representation of the transform method applied to the evaluation of the Jacobian as the forcing term for spectral components Q_{kl} .

demands only $N \log N$ operations for N Fourier modes and N grid points. In two dimensions, we first perform N FFTs along the x -direction, one for each of the y values. Each of these N transforms costs $N \log N$ operations, and we thus perform $N^2 \log N$ operations. We then perform N FFTs of the latter coefficients in the other direction, requiring another $N^2 \log N$ operations. In total, $N^2 \log N^2$, or in terms of the total number M of unknowns, $M \log M$ operations are needed for one passage from physical domain to spectral space or vice versa. With M operations needed for the calculation of the Jacobian by products in physical space, the chief cost is that of the transformation, but this is less than if the Jacobian had been computed in the spectral space, at the cost of M^2 calculations. The larger M (and M must be large indeed to achieve high resolution), the greater the reduction of operations.

The transform method can, of course, be generalized to any other term that is not easily calculated in spectral space, such as nonlinear source terms for tracers. All that needs to be done is to pass from spectral space to physical domain using an FFT scheme, calculate those complicated terms on the spatial grid and then return to spectral space by the inverse transformation.

Convergence of the truncated spectral series to exact solutions can be shown to be faster than any power of M as long as the solution is smooth for all derivatives. This makes the method extremely attractive. We note in passing that we found a way to solve a classical Poisson equation on a periodic domain with $M \log M$ operations through the transform approach.

Unfortunately, the advantage of the transform method is partially mitigated by a drawback, the aliasing due to products in physical space. As seen in Section 10.5, for a grid spacing of Δx , we can avoid any aliasing in the quadratic terms if modes with wavelengths between $2\Delta x$ and $3\Delta x$ are systematically removed from the solution. But removing modes downgrades resolution, and the requirement must be turned the other way round: For the shortest wavelength λ that needs to be resolved, we have to create a physical grid such that $\Delta x = \lambda/3$ instead of $\Delta x = \lambda/2$, the strict minimum needed to resolve λ . On this grid, the amplitudes of projected modes between $2\Delta x$ and $3\Delta x$ are absent by construction, and no aliasing can occur when computing quadratic terms. In other words, we simply have to use $3/2N$ grid points instead of N to be sure that the product in physical space does not lead to nonlinear numerical instabilities. In practice, such a generation of a higher-resolution sampling can be performed efficiently by first padding with $N/2$ zeros the arrays containing Fourier coefficients and then applying the transformation. This amounts to assigning zero amplitudes to higher-wavenumber signals and then calculating the resulting series expansions on a regular grid with $3N/2$ points using standard FFTs (see Appendix C). This method of proceeding permits to retain the advantage of a spectral method while avoiding aliasing.

An additional advantage of working in spectral space lies in the fact that spectral analysis of the results is trivial and that the power spectrum of initial conditions is easily controlled. This is particularly useful for statistical analysis of geostrophic turbulence which starts from a random field of known

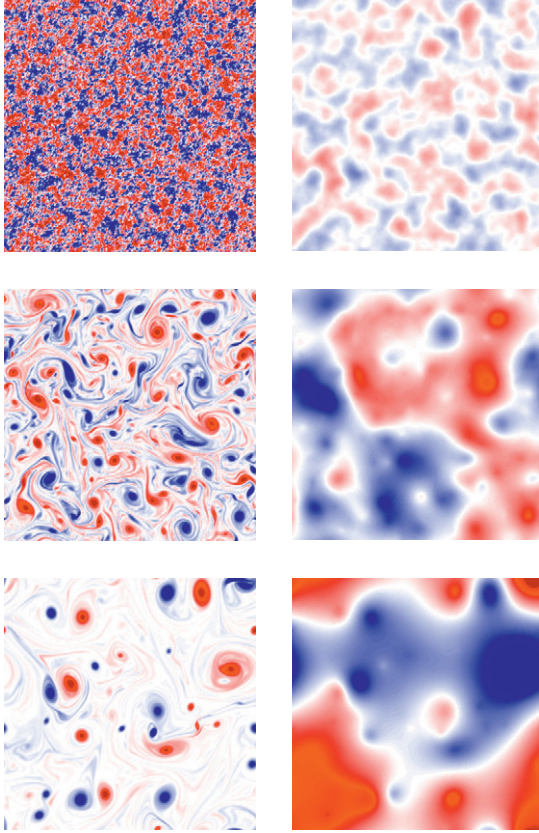


FIGURE 18.17 Emergence of isolated vortices from a random initial field. Vorticity (left) and streamfunction (right) in a periodic domain at three successive moments. The simulation was performed with a spectral method implemented in `qgspectral.m`.

statistical spectral profile. Generally, the fields are generated as a realization of random streamfunctions with a Gaussian distribution of zero mean and variances depending on wavenumbers. Simulations then allow to see how vortices become organized under different dissipation conditions (Fig. 18.17) and how power spectra evolve.

ANALYTICAL PROBLEMS

- 18.1.** Consider the center fluid parcel ($y=0$) of the Gaussian jet $u(y) = U \exp(-y^2/2L^2)$ with $U = 10$ m/s and $L = 100$ km. On the f -plane, what is the shear vorticity acquired by that parcel in a rightward meander of curvature $\mathcal{K} = 1/800$ km? On the beta plane, what meridional

displacement Y would permit the parcel to conserve its speed and maintain its center position?

- 18.2.** For the one-layer reduced gravity model (12.19), express the gradient-wind balance for steady circular vortices on the f -plane. If the layer thickness is H at the center, and the density interface outcrops at radius a [i.e., $h(r=0)=H$, $h(r=a)=0$], show that H and a must satisfy the inequality

$$a \geq \frac{\sqrt{8g'H}}{f}. \quad (18.43)$$

- 18.3.** Take a stretch of the jet profile $u(y) = U(1 - |y|/a)$ in $|y| \leq a$, $u(y) = 0$ elsewhere (see Fig. 10.13), and bend it to create a clockwise vortex. On the f -plane and in the absence of vertical variations, what is the orbital-velocity profile that preserves vorticity on every trajectory? How does the pressure anomaly in the vortex is compared with the pressure difference across the jet? Finally, show that the proportion of fluids with each vorticity is the same in the vortex as in the straight jet.
- 18.4.** Determine the behavior of an eastward jet in the northern hemisphere flowing over a topographic step-up followed by a step-down of equal height. Is the flow oscillatory beyond the second step? Also discuss the cases where the distance between the two steps is short and long compared with the critical meander scale.
- 18.5.** Redo Problem 18.4 for a westward jet in the southern hemisphere.
- 18.6.** Hurricane Hugo (10–22 September 1989 in the western North Atlantic—see Fig. 18.18) had a maximum wind speed of 62 m/s and a low central pressure of 941.4 millibars during its passage over Guadeloupe on 17 September (Case & Mayfield, 1990). Assuming that the normal pressure outside the hurricane was 1010 millibars, estimate the storm's radius and importance of the centrifugal force relative to the Coriolis force (latitude = 16°N).
- 18.7.** Using the gradient-wind balance (18.11) in a reduced-gravity model ($p = \rho_0 g' h$), explore lens-like vortex solutions where the interface exhibits a paraboloidal shape between a central maximum depth ($h = H$ at $r = 0$) and a peripheral outcrop ($h = 0$ at $r = R$). Show that the flow is in solid-body rotation. Relate vortex radius R to central depth H and discuss the limiting cases of wide/shallow and narrow/deep vortices. Do you recover an inequality of type (18.16)?
- 18.8.** In first-approximation, the thick atmosphere of Jupiter may be modeled as a reduced-gravity system with $g' = 2.64 \text{ m/s}^2$. Knowing that planet radius is 69,000 km, and that one Jovian day is only 10 Earth hours long,

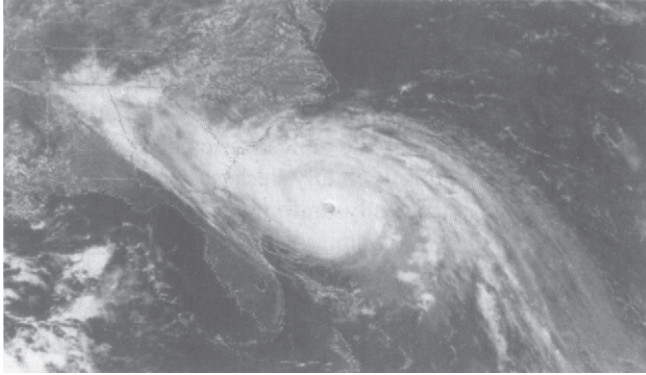


FIGURE 18.18 Satellite visible image of Hurricane Hugo in the evening of 21 September 1989 as it approached the south-eastern coast of the United States. (Courtesy of NOAA, Department of Commerce, Washington, D.C.)

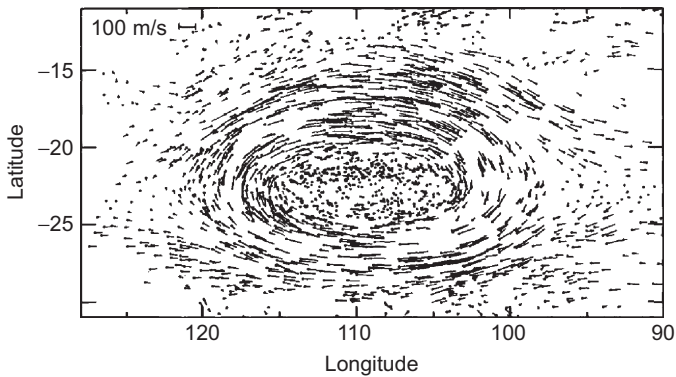


FIGURE 18.19 Velocity field on Jupiter in and around the Great Red Spot, obtained after tracking small cloud features in sequential images from *Voyager* spacecraft. The origin of each vector is indicated by a dot. (From Dowling & Ingersoll, 1988)

derive the thickness h of moving fluid for a few radial sections across the wind-velocity chart provided in Fig. 18.19.

- 18.9.** A uniform eastward flow of velocity U over a flat bottom approaches a topographic step at right angle. Topography changes from H_0 to H_1 at $x = 0$. Determine the stationary streamfunction for $x > 0$ under the rigid-lid approximation and on the beta plane. Can you identify the critical meander scale in the solution? (*Hint:* On a streamline, potential vorticity is conserved. Express that at the step the relationship between the value of the streamfunction and vorticity is known and is thus valid beyond the step.)

18.10. Redo [Analytical Problem 18.9](#) for a westward flow.

18.11. Prove [Eq. \(18.7\)](#). (*Hint:* Use Frenet coordinates.)

NUMERICAL EXERCISES

18.1. Use `qgspectral.m` to experiment with different eddy fields. Then include the beta effect and higher-order dissipation using sixth-order derivatives.

18.2. Include diagnostics on energy, enstrophy, and wavelength into `qgspectral.m` and simulate with different eddy viscosity values. Also include diagnostics on

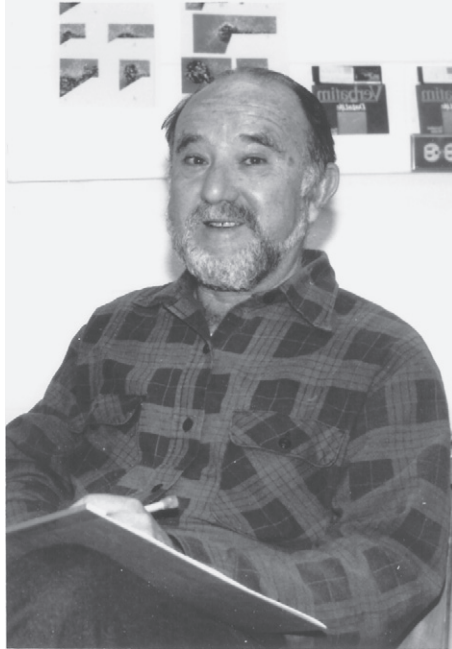
$$k_e = \frac{\int k |k\Psi_k|^2 dk}{\int |k\Psi_k|^2 dk} \quad (18.44)$$

$$k_o = \frac{\int k |Q_k|^2 dk}{\int |Q_k|^2 dk}, \quad (18.45)$$

where integrals are performed over all wavenumbers $k = \sqrt{k_x^2 + k_y^2}$. Look at the time evolution of these quantities and provide an interpretation.

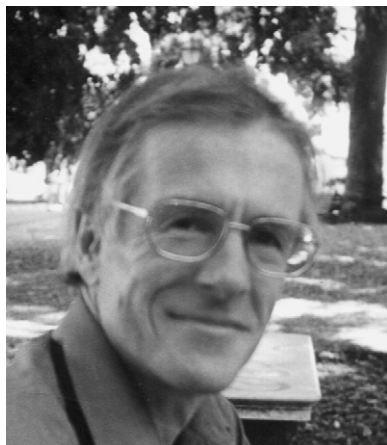
18.3. Generalize `qgspectral.m` to a two-layer system with equations given in (17.31). In particular, mind the vertical coupling in (17.32) and solve the coupled problem in spectral space exactly. Vary the parameter R to explore the effect of vertical stratification.

Melvin Ernest Stern
1929–2010



Melvin Stern was an important contributor to the GFD Summer Program at the Woods Hole Oceanographic Institution (see historical note at the end of Chapter 1) and had a major influence on the evolution of the field ever since the inception of that program. His early work in meteorology was followed by fundamental contributions to our understanding of baroclinic instability (work with Jule Charney) and of salt fingering (an oceanic small-scale diffusive process). After publishing a book titled *Ocean Circulation Physics* (Academic Press, 1975), Stern dedicated an increasing amount of time and effort to the investigation of vortices. He is credited with the *modon* solution (Section 16.6), and seminal studies of jets and jet-vortex interactions, complementing his theoretical results with original and illuminating laboratory experiments. (*Photo by the first author*)

Peter Douglas Killworth
1946–2008



A student of Adrian Gill (see Biography at the end of Chapter 13), Peter Killworth, made a career of touching on almost all aspects of ocean modeling. He is renowned for his contributions to both theoretical oceanography, including wave and stability analysis, and numerical model developments. His breadth of interests went as far as social networks, which he analyzed using mathematical and modeling skills that he cultivated while working on oceanographic problems.

In addition, Killworth gained a reputation as an extremely incisive and responsive editor from authors and reviewers of *Ocean Modelling*. He was awarded numerous honors “for his many far-reaching contributions to theoretical oceanography, which have significantly enlarged our understanding of the processes determining ocean circulation.” (Photo by Sarah Killworth)